Ran, H, Ma, J, Chen, X, Sun, Y, Gkantou, M and McCrum, D

Local Stability of Laser-Welded Stainless-Steel T-Section Stub Columns

Local stability of laser-welded stainless steel T-section stub columns

Hongdong Ran [a,b], Jing Ma [a], Xiangrong Chen [a,b], Yao Sun [c,*], Michaela Gkantou [d], Daniel McCrum [e]

[a] School of Civil Engineering, Xi'an University of Architecture and Technology, Xi'an 710055, China.

[b] Key Lab of Structural Engineering and Earthquake Resistance, Ministry of Education (XAUAT), Xi'an 710055, China

[c] College of Civil Engineering, Hunan University, Changsha 410082, China.

[d] School of Civil Engineering and Built Environment, Liverpool John Moores University, Liverpool L3 3AF, UK.

[e] School of Civil Engineering, University College Dublin, Dublin D04 V1W8, Ireland.

* Corresponding author, Email: yaosun@hnu.edu.cn

Abstract: This paper reports an experimental and numerical study on the local stability and compression resistance of laser-welded stainless steel T-section stub columns. An experimental program was first conducted, comprising material coupon tests, residual stress measurements and twenty stub column tests. Upon completion of the laboratory experiments, a numerical modeling program was carried out, where finite-element models were established and validated. The validated finite-element models were then used to perform parametric analyses to derive more numerical data. The obtained numerical and test data were employed to undertake an in-depth design analysis, where the relevant design provisions in the American and European standards as well as the continuous strength method were examined. The design analysis results indicate that the American and European standards lead to significant inaccuracies of the ultimate load predictions, especially for laser-welded stainless steel non-slender T-sections,

owing to no consideration of material strain hardening, while the continuous strength method is shown to provide greatly improved design consistency and accuracy over the current American and European standards.

Keywords: Stub column test; Design code; Laser-welded T-section; Stainless steel, Effective width method; Continuous strength method.

1. Introduction

In recent years, stainless steel has gained extensive utilization in various fields such as bridge and offshore engineering [1–3]. This popularity is attributed to its favorable mechanical attributes, coupled with outstanding durability and resistance to corrosion, resulting in a substantial reduction in the necessity for inspection and maintenance efforts. As an advanced manufacturing method, laser welding has the capability to reduce input heat effectively, thereby resulting in minimal thermal distortions and residual stresses [4]. As a result, the use of laser welding has seen a growing trend in joining stainless steel components to create a diverse range of built-up sections. Research work on laser-welded stainless steel (LWSS) components with different cross-sections and subjected to different loading conditions has been performed, aimed at verifying their structural behavior, examining the applicability of codified design provisions and formulating improved design approaches. Gardner et al. [5] performed laboratory tests on LWSS non-slender I-section stub columns, aimed at investigating their local stability and compressive strengths, while the behavior of their slender counterparts was experimentally examined by Ran et al. [6]. Theofanous et al. [7] and Bu and Gardner [8] performed in-plane bending tests on LWSS angle, channel and I-section beams, aimed at studying their bending behavior. Liang et al. [9,10] experimentally explored the local buckling response of LWSS channels subject to combined loading. The global stability of LWSS angle and I-section columns was examined by Filipović et al. [11], and Gardner et al. [5] through a series of pin-ended column experiments. A testing program was carried out by Bu and Gardner [12] on LWSS beam-columns with non-slender I-sections to explore their structural performance, while the global stability of their slender counterparts was experimentally investigated by Ran et al. [13]. This literature review indicated that although comprehensive research on LWSS structural members has been previously conducted, the behavior and strengths of LWSS T-sections remain unexplored; this investigation is thus prompted.

In this study, a laboratory testing program, comprising material coupon tests, residual stress measurements and twenty stub column tests, was first conducted (Section 2). The experimentally acquired data were analyzed and employed in a numerical modeling program for establishing and validating finite-element (FE) models (Section 3). Based on the completion of validation, the FE models were adopted to carry out systematic parametric studies to generate additional numerical data. On the basis of the acquired numerical and test data, the design provisions in AISC 370 (AISC) [14] and EN 1993-1-4 (EC3) [15] and the continuous strength method (CSM) [16] for LWSS T-sections under compression were evaluated (Section 4).

2. Testing program

2.1. Overview

A testing program was initially conducted in order examine the compressive behavior and strengths of LWSS T-sections. Five T-section profiles were adopted in this program, with three different thicknesses considered for each profile, resulting in a total of fifteen T-section sizes, as presented in Table 1. They were manufactured by laser welding from EN 1.4301 austenitic stainless steel sheets, with the welding procedures and techniques satisfying those prescribed in ISO 13919 [17]. The T-sections have been carefully selected to cover both non-slender (Class 1–3) and slender (Class 4) cross-sections, according to both the AISC and EC3 cross-section classification frameworks [14,15]. Twenty stub column specimens were fabricated. The geometric sizes of each specimen were measured, involving the specimen length L, the flange width b_f, the section outer height h, the web height h_w and the plate thickness t (see Fig. 1), as presented in Table 1. The overall testing program comprises material tests, residual stress measurements and twenty stub column tests. Detailed descriptions of the key observations and the adopted procedures and setups are provided in the following sub-sections.

2.2. Material testing

Material testing was performed to obtain the material properties of the austenitic stainless steel used. Six material coupons were extracted longitudinally from the three batches of original sheets with the thicknesses of 3 mm, 5 mm and 8 mm, with two coupons for each thickness. Their geometries were in accordance with the specifications of ISO 6892 [18]. The coupons were tested using a 250 kN displacement-controlled universal machine. The test rig is shown in Fig. 2, where an extensometer with a 50 mm gauge length is attached to the central portion of the coupon and two strain gauges are affixed to the coupon. The initial loading rate was set to 0.04 mm/min and subsequently increased to 0.35 mm/min when the 0.2% proof strength was attained. Fig. 3 gives the stress–strain curves obtained from the material testing, while the key material properties, involving the 0.2% and 1.0% proof strengths $\sigma_{0.2}$ and $\sigma_{1.0}$, the ultimate strength σ_u, the Young's modulus E, the strains respectively at the ultimate stress and fracture ε_u and ε_f, and the R–O parameters n and $m_{1.0}$ [19–21], are averaged and summarized in Table 2.

2.3. Residual stress measurements

Residual stresses are inevitably introduced into the steel sections during the welding process, which may result in premature failure of the structural members [22]. The residual stresses in the studied LWSS T-sections were therefore measured through the sectioning method. This method has been successfully employed in previous measurements of residual stresses in different welded sections [5,6,23–28]. A total of six sets of residual stress measurements were conducted on T-sections with the T-90×90 profiles, with two repeated measurements for each plate thickness. Fig. 4 shows the locations and dimensions of the strips cut for the residual stress measurements; each strip is nominally 300 mm long and 9 mm wide. Prior to sectioning, two gauge holes with a diameter of 2 mm were drilled along the centerline of the exterior face of each strip and at a distance of 25 mm from the strip ends, through the use of an automatic dot puncher, leading to the nominal length between the gauge holes L_0 equal to 250 mm; the actual strip length between the two gauge holes was thereafter measured using a Demec gauge with 250 mm gauge length. Upon length measurements of strips within the T-sections, each specimen was cut into strips, allowing for the release of residual stresses. A typical sectioned T-90×90×3 specimen is shown in Fig. 5. The Demec gauge was again adopted for the length measurements of strips between the gauge holes after sectioning. For each strip, the readings of the Demec gauge taken before and after sectioning are respectively denoted as r_1 and r_2. Hence, the strain ε_{rs} induced by the release of residual stress is calculated as $(r_2–r_1)/L_0$ and the residual stress σ_{rs} can be back-calculated as $E\cdot\varepsilon_{rs}$.

The six measured sets of residual stresses are presented in a normalized format ($\sigma_{rs}/\ \sigma_{0.2}$) in Fig. 6, which are shown to be in good agreement. Note that there are no codified residual stress predictive models for welded T-sections, whilst the Swedish regulations BSK 99 [29] and European convention ECCS [30] set out predictive models, as shown in Fig. 7 and Table 3. The models are for carbon steel welded I-sections, which can be considered to be geometrically composed of two T-sections. The BSK and ECCS models are plotted in Fig. 6, with their applicability to LWSS T-sections evaluated. It can be seen that the LWSS T-sections contain much lower peak residual stresses than the corresponding predictions from the codified models; this may be attributed to the fact that laser welding can greatly reduce input heat, thereby resulting in lower residual stresses. Moreover, it is observed that the flange tip of T-section has tensile residual stresses, which are contradictory to the compressive residual stress predictions from the codified models. The same finding has been reported in previous studies [23,25,31] on residual stresses in carbon steel welded T-sections. Therefore, the two codified predictive models are proven to be unsuitable for LWSS T-sections. A new predictive model is proposed herein, as defined in Fig. 8 and Table 4, revealing an excellent agreement with the measured residual stress data points.

2.4. Stub column tests

For the purpose of investigating the local stability and strengths of LWSS T-sections under compression, stub column tests were conducted on the twenty T-section specimens. All the stub column specimens were tested in a universal machine, which applied concentric compression forces to the specimen ends. It is worth noting that the nominal stub column length was selected in accordance with the recommendations given in Ziemian [32], and set to be equal to three times the outer section height herein; the selected specimen lengths are short enough to prevent the occurrence of member global buckling, but still sufficiently long to incorporate representative residual stress distributions and initial geometric imperfection patterns. Each specimen was initially milled to achieve flat ends and then thoroughly deburred to guarantee a uniform compressive stress distribution on the stub columns during testing. Before testing, the initial local geometric imperfections ω_0 of the specimens were measured using a percentage gauge (see Fig. 9), with the measurement procedures in line with those used in previous imperfection measurements [5–10,28,33], and are tabulated in Table 1. Fig. 10 exhibits the main instrumentation adopted in each stub column test, involving four LVDTs and four strain gauges. The strain gauges were affixed to the mid-height faces of the web and flange to measure the corresponding axial strains, while four LVDTs are positioned at the specimen ends to record the end-shortening. Once the test setup was completed, a loading speed of 0.2 mm/min was adopted to drive the universal machine to concentrically compress each test specimen, and all data, comprising the compression loads, the longitudinal strains and the end-shortenings, were simultaneously recorded through using a data acquisition system DATASCAN at an interval of one second. Fig. 11 illustrates the full load versus end-shortening responses for the twenty stub columns, grouped by specimen cross-section profiles, while Table 1 presents the key experimental results, involving the ultimate loads N_u and the corresponding end-shortening δ_u. Finally, the failure modes of five representative LWSS T-section stub column specimens are displayed in Fig. 12, featuring significant local buckling.

3. Numerical modeling

3.1. Overview

For the purpose of supplementing the laboratory experiments and expanding the acquired data pool, numerical simulations were performed using the ABAQUS FE package [34]. The modeling procedures and techniques used to develop the FE models are first described, followed by a detailed description of a validation study, which compared the established FE model data to the test results. Upon validation, the FE models were adopted and used to perform parametric analyses over a broader range of cross-sectional sizes and aspect ratios.

3.2. Establishment and validation of FE models

As provided in the ABAQUS element library [34], the 'S4R' shell element has been used for simulating a variety of stainless steel members [6,8–10,12,13,24] and was used herein. Through a prior mesh sensitivity investigation, the element size was selected as t. This size was found to (i) enable accurate modeling of residual stresses and (ii) result in proper computational efficiency and accuracy. The engineering material response, acquired from the material testing, was transformed to the true response [6,8] and afterwards used in the FE modeling. Since the performance of thin-walled steel components may be affected by residual stresses, they were incorporated into the FE models utilizing the 'INITIAL CONDITION' command [34], with their amplitudes and patterns acquired from the predictive model shown in Fig. 8. Fig. 13 illustrates the residual stresses included in the modeled specimen T-60×60×3.

The fixed-ended boundary conditions were precisely represented in the FE models using constraints. Each end section was coupled to one concentric reference point. The bottom reference point was restrained with no degree of freedom allowed, whilst its top counterpart has longitudinal translation only – see Fig. 13. Incorporation of initial local geometric imperfections was also completed for each stub column FE model. Specifically, an elastic eigenvalue analysis [34] was initially performed for acquiring the lowest local buckling mode of each FE model, which was adopted as the imperfection profile and factored by the corresponding measured imperfection amplitude, according to Table 1.

Once the FE models were built, the nonlinear analysis 'Static, Riks' [34] was used to acquire the numerical response, comprising numerical failure modes and loads as well as load–end-shortening histories. The accuracy of the numerical results from the FE models was examined through comparison with the experimental results. Graphical comparisons between the numerical and test load–deformation histories for the twenty tested stub columns are displayed in Fig. 11, in which the experimental responses are found to be precisely captured by their FE counterparts. The effect of residual stresses on the local stability of LWSS T-sections was also evaluated by comparing the FE load–deformation histories with and without residual stresses, with the results shown in Fig. 14. It can be seen from the figure that the FE load–deformation histories with residual stresses almost coincide with their counterparts without residual stresses, indicating the insignificant effect of residual stresses [9,10]. The mean test-to-FE ultimate load ratio is equal to 1.01, demonstrating that the developed FE models can provide very good predictions of the ultimate loads. In addition to the good agreements between the numerical and test load–deformation histories and ultimate loads, the experimental failure modes were also accurately simulated by the FE models, as depicted in Fig. 15 for two typical specimens. Overall, the established FE models were shown to simulate well the performance of LWSS T-sections under compression and therefore demonstrated to be validated.

3.3. Parametric analyses

Upon validation of the FE models, systematic parametric analyses were conducted, aimed at expanding the data bank over a broader spectrum of cross-sectional sizes and aspect ratios, beyond those examined in the testing program. For the modeled T-sections, their geometric dimensions were selected carefully to ensure that all cross-section classes are covered, accounting for both the AISC and EC3 cross-section classification frameworks [14,15]. Specifically, the web heights and flange widths ranged from 60 and 200 mm and the thicknesses from 3 to 12 mm, enabling an extensive spectrum of cross-sectional geometries to be examined. All modeled stub columns were developed using the aforementioned modeling techniques, procedures as well as assumptions. In total, numerical data for 169 LWSS T-section stub columns were acquired through parametric analyses.

4. Design analysis

4.1. Overview

Based on the laboratory experiments and numerical simulations, a comprehensive design analysis is conducted in this section. The design provisions prescribed in AISC 370 [14] and EN 1993-1-4 [15] for LWSS T-sections under compression are first described, and their suitability is assessed using the numerical and experimental data. The conservatism of the AISC 370 and EN 1993-1-4 design provisions is revealed and discussed. The CSM [16], as an alternative design method, is then evaluated, with design prediction improvement observed. The quantitative assessments of the three design methods [14–16] are presented in Table 5, where the mean FE/test-to-predicted ultimate load ratios $N_u/N_{u,pred}$, and their COVs are reported. Figs 16–20 give the graphical assessment results on the basis of the numerical and test data.

4.2. AISC 370

AISC 370 [14] is a recently developed American specification in for stainless steel structures. For T-sections under compression, two section classes are set out in AISC 370 [14], including non-slender T-sections and slender T-sections. The classification of T-sections is conducted by comparing the width-to-thickness ratio of the most slender plate element $\lambda_{max,AISC}$ with the codified limiting width-to-thickness ratio of $\lambda_r=0.41(E/\sigma_{0.2})^{0.5}$. For non-slender T-sections, their compression resistance is defined as the cross-sectional yield load $N_y=A\sigma_{0.2}$. Slender T-sections are susceptible to local buckling that reduces the effectiveness of the full cross-section. To allow for the local buckling effect, the effective width approach is adopted in AISC 370 [14].

Specifically, a reduction factor ρ_{AISC} is introduced to reduce the original plate width to the effective plate width, as defined by Eq. (1), where f_{el} is the elastic local buckling stress of the cross-section, as calculated from Eq. (2), where v is the Poisson's ratio and equal to 0.3 for stainless steel, and λ is the width-to-thickness ratio and equal to $\lambda_{w,AISC}=(h_w+t)/t$ for web and $\lambda_{f,AISC}=0.5b_f/t$ for flange. A worked example is presented in Appendix A to further demonstrate the calculation procedures of AISC 370 [14].

$$\rho_{AISC}=0.772\left(1-0.10\sqrt{\frac{f_{el}}{\sigma_{0.2}}}\right)\sqrt{\frac{f_{el}}{\sigma_{0.2}}} \tag{1}$$

$$f_{el}=\frac{0.425\pi^2E}{12\left(1-v^2\right)\lambda^2} \tag{2}$$

Based on the FE and test results, the suitability of the AISC design provisions for LWSS T-sections under compression is assessed. The numerically and experimentally obtained ultimate loads N_u are normalized by the section yield loads N_y and plotted against the width-to-thickness ratio of the most slender plate element $\lambda_{max,AISC}$ (taken as the greater value of $\lambda_{w,AISC}$ and $\lambda_{f,AISC}$) in Fig. 16. It can be seen from the figure that the current AISC limiting web-to-thickness ratio λ_r is conservative when used for classifying LWSS non-slender and slender T-sections. A new limiting ratio $\lambda_{r,p}=0.41(E/\sigma_{0.2})^{0.5}$ is then proposed to improve the accuracy of cross-section classification, as also depicted in Fig. 16. Regarding the accuracy of the AISC design compressive resistance $N_{u,AISC}$, a quantitative assessment is undertaken, with the results, involving the mean ultimate load ratios $N_u/N_{u,AISC}$ and the COVs, given in Table 5(a). The results show an under-estimation of the mean capacity ($N_u/N_{u,AISC}$=1.20) and considerable inconsistency, especially for non-slender T-sections (COV=0.067). The conservatism is also observed in Fig. 17, where the load ratios $N_u/N_{u,AISC}$ are plotted against the width-to-thickness ratio of the most slender plate element $\lambda_{max,AISC}$. The graphical assessment evidently demonstrates that the American specification yields rather scattered and conservative strength predictions for LWSS T-sections under compression, due to the ignorance of material strain hardening.

4.3. EN 1993-1-4

EN 1993-1-4 [15] is a European code established specifically for stainless steel structures. Similar to its American counterpart AISC 370, the Eurocode also adopts the cross-section classification framework, which categorizes cross-sections in compression into non-slender (Class 1–3) and slender (Class 4) sections. For a T-section under compression, its class is determined by comparing the slenderness of its most slender element $\lambda_{max,EC3}$ (taken as the greater value of $\lambda_{w,EC3}=h_w/t$ and $\lambda_{f,EC3}=0.5(b_f–t)/t$) against the Class 3 slenderness limit $\lambda_s=11.5\cdot(235/\sigma_{0.2})^{0.5}$. The Class 3 slenderness limit is graphically evaluated in Fig. 18 based on the test and FE results for LWSS T-sections, showing high accuracy. Upon completion of the cross-section classification, EN 1993-1-4 [15] prescribes the cross-sectional yield load and effective load as the design resistance $N_{u,EC3}$ for non-slender T-sections and slender T-sections under compression, respectively. The cross-sectional effective load is determined from the effective width approach, as expressed by Eq. (3), in which λ_p is the element slenderness and can be determined from Eq. (4), where λ_1 is equal to $\lambda_{w,EC3}=h_w/t$ for web and $\lambda_{f,EC3}=0.5(b_f–t)/t$ for flange. The calculation procedures of EN 1993-1-4 [15] are detailed in a worked example given in Appendix A.

$$\rho_{EC3} = \frac{0.655\lambda_p - 0.013}{\lambda_p^{\;2}} \tag{3}$$

$$\lambda_p = \frac{\lambda_1}{18.2\sqrt{235/\sigma_{0.2}}} \tag{4}$$

The EC3 design provisions are quantitatively and qualitatively assessed based on the FE and test results. The quantitative assessment results, comprising the mean ultimate load ratio $N_u/N_{u,EC3}$ and COVs, are summarized in Table 5(b), indicating slightly improved design accuracy in comparison with the assessment results of AISC 370 [14]. However, the quantitative assessment also reveals the design conservatism of EN 1993-1-4 [15] for non-slender T-sections under compression ($N_u/N_{u,EC3}$=1.23), which is also found from the qualitative assessment in Fig. 19. This may be attributed to that material strain hardening, which is not considered in the design.

4.4. CSM

The results presented in Sections 4.2 and 4.3 show that the current American and European standards [14,15] lead to conservative strength predictions, especially for LWSS non-slender T-sections, due to the neglect of material strain hardening. To address the inherent conservatism, the CSM [16] that rationally considers strain hardening has been incorporated into the new edition of Eurocode EN 1993-1-4 [14] as an alternative design method. To calculate the CSM cross-section capacity, the first step lies in quantification of the CSM strain limit ε_{csm} that reflects the deformation capacity of the examined T-section under compression; this can be attained by employing the 'base curve', expressed by Eq. (5), in which $\varepsilon_y=\sigma_{0.2}/E$ is the elastic strain at the yield strength, $\lambda_{p,cs}=(\sigma_{0.2}/\sigma_{cr,cs})^{0.5}$ is the cross-section slenderness, where $\sigma_{cr,cs}$ denotes the elastic local buckling stress of the full T-section under compression and can be identified utilizing the finite-strip package CUFSM [35]. Once the CSM strain limit ε_{csm} is quantified, the CSM cross-section compression capacity $N_{u,csm}$ is determined by utilizing Eq. (6), where E_{sh} is the strain hardening modulus, as given by Eq. (7), in which $\varepsilon_{u,csm}=1-\sigma_u/\sigma_{0.2}$ is the CSM ultimate strain. The application of the CSM [16] is demonstrated in detail through a worked example given in Appendix A.

$$\frac{\varepsilon_{csm}}{\varepsilon_y}=\begin{cases}\dfrac{0.25}{\lambda_{p,cs}^{\;3.6}}\leq\min\left(15,\dfrac{0.1\varepsilon_u}{\varepsilon_y}\right) & \text{for } \lambda_{p,cs}\leq 0.68\\[2ex] \left(1-\dfrac{0.222}{\lambda_{p,cs}^{\;1.05}}\right)\dfrac{1}{\lambda_{p,cs}^{\;1.05}} & \text{for } \lambda_{p,cs}>0.68\end{cases} \tag{5}$$

$$N_{u,csm}=\begin{cases}A\sigma_{0.2}\dfrac{\varepsilon_{csm}}{\varepsilon_y} & \text{for } \dfrac{\varepsilon_{csm}}{\varepsilon_y}\leq 1.0\\[2ex] A\sigma_{0.2}+AE_{sh}\varepsilon_y\left(\dfrac{\varepsilon_{csm}}{\varepsilon_y}-1\right) & \text{for } \dfrac{\varepsilon_{csm}}{\varepsilon_y}>1.0\end{cases} \tag{6}$$

$$E_{sh}=\frac{\sigma_u-\sigma_{0.2}}{0.16\varepsilon_{u,csm}-\varepsilon_y} \tag{7}$$

The numerical and test ultimate loads N_u are normalized by the corresponding CSM strengths, $N_{u,csm}$, and plotted against the cross-section slenderness $\lambda_{p,cs}$ in Fig. 20, in which the CSM is shown to be capable of predicting well the FE and test ultimate loads. The graphical evaluation is followed by a quantitative evaluation, with the results given in Table 5(c), where the mean load ratios $N_u/N_{u,csm}$ for non-slender and slender T-sections are equal to 1.08 and 1.04, respectively. The quantitative and graphical evaluations demonstrated that the CSM provides greatly improved design accuracy over AISC 370 and EN 1993-1-4 for LWSS T-sections under compression, due mainly to the rational consideration of strain hardening.

5. Conclusions

The local stability and load-carrying capacity of LWSS T-sections under compression have been examined through laboratory experiments and numerical simulations. An experimental program, involving twenty stub column tests and supplementary material tests and residual stress measurements, was first conducted. The laboratory experiments were complemented by numerical modeling, with FE models built and validated with reference to the test response. Upon validation, the FE models were utilized in parametric analyses, enabling additional data to be generated over an extensive variety of cross-sectional aspect ratios and dimensions. The numerical data, in combination with the test results, were utilized for assessing the design provisions prescribed in AISC 370 [14] and EN 1993-1-4 [15]. The results show that the codified curves yield conservative predictions of ultimate strength, owing to the neglect of material strain hardening. In particular, on the basis of the experimental and numerical results of this study, $N_u/N_{u,AISC}$ was found to have a mean value of 1.20, while $N_u/N_{u,EC3}$, a mean value of 1.18. The CSM [16] that has been incorporated into the new edition of EN 1993-1-4 as an alternative design method was also examined. The CSM is evidenced to be able to yield more consistent (COV=0.045) and accurate ($N_u/N_{u,csm}$=1.06) ultimate load predictions than its AISC 370 and EN 1993-1-4 counterparts.

References

[1] Baddoo, N. R. (2008). Stainless steel in construction: A review of research, applications, challenges and opportunities. Journal of Constructional Steel Research, 64(11), 1199-1206.

[2] Gedge, G. (2008). Structural uses of stainless steel—buildings and civil engineering. Journal of Constructional Steel Research, 64(11), 1194-1198.

[3] Gardner, L. (2019). Stability and design of stainless steel structures–Review and outlook. Thin-Walled Structures, 141, 208-216.

[4] Ragavendran, M., & Vasudevan, M. (2021). Effect of laser and hybrid laser welding processes on the residual stresses and distortion in AISI type 316L (N) stainless steel weld joints. Metallurgical and Materials Transactions B, 52(4), 2582-2603.

[5] Gardner, L., Bu, Y., & Theofanous, M. (2016). Laser-welded stainless steel I-sections: Residual stress measurements and column buckling tests. Engineering Structures, 127, 536-548.

[6] Ran, H., Chen, Z., & Ma, Y. (2022). Experimental and numerical studies of laser-welded slender stainless steel I-section columns. Thin-Walled Structures, 171, 108832.

[7] Theofanous, M., Liew, A., & Gardner, L. (2015). Experimental study of stainless steel angles and channels in bending. Structures, 4, 80-90.

[8] Bu, Y., & Gardner, L. (2018). Local stability of laser-welded stainless steel I-sections in bending. Journal of Constructional Steel Research, 148, 49-64.

[9] Liang, Y., Zhao, O., Long, Y. L., & Gardner, L. (2019). Stainless steel channel sections under combined compression and minor axis bending–Part 1: Experimental study and numerical modelling. Journal of Constructional Steel Research, 152, 154-161.

[10] Liang, Y., Zhao, O., Long, Y. L., & Gardner, L. (2020). Experimental and numerical studies of laser-welded stainless steel channel sections under combined compression and major axis bending moment. Thin-Walled Structures, 157, 107035.

[11] Filipović, A., Dobrić, J., Buđevac, D., Fric, N., & Baddoo, N. (2021). Experimental study of laser-welded stainless steel angle columns. Thin-Walled Structures, 164, 107777.

[12] Bu, Y., & Gardner, L. (2019). Laser-welded stainless steel I-section beam-columns: Testing, simulation and design. Engineering Structures, 179, 23-36.

[13] Ran, H., Chen, Z., Ma, Y., OBrien, E., & Sun, Y. (2023). Experimental and numerical study of laser-welded stainless steel slender I-section beam-columns. Engineering Structures, 286, 116128.

[14] ANSI/AISC 370-21. (2021). Specification for Structural Stainless Steel Buildings, American Institute of Steel Construction (AISC).

[15] prEN 1993-1-4:2021. (2021). Eurocode 3: Design of steel structures — Part 1-4: General rules – supplementary rules for stainless steels. European Committee for Standardization (CEN), Brussels.

[16] Gardner, L., Yun, X., & Walport, F. (2023). The continuous strength method–Review and outlook. Engineering Structures, 275, 114924.

[17] ISO 13919-1:2019. (2019). Electron and laser-beam welded joints – Requirements and recommendations on quality levels for imperfections – Part 1: Steel, nickel, titanium and

their alloys. European Committee for Standardization (CEN), Brussels.

[18] EN ISO 6892-1: 2016. (2016). Metallic materials: Tensile testing – Part 1: Method of test at room temperature. European Committee for Standardization (CEN), Brussels.

[19] Ramberg, W., & Osgood, W.R. (1943). Description of stress–strain curves by three parameters. National Advisory Committee for Aeronautics (NACA), Technical note, 902, Washington.

[20] Rasmussen, K. J. (2003). Full-range stress–strain curves for stainless steel alloys. Journal of Constructional Steel Research, 59(1), 47-61.

[21] Arrayago, I., Real, E., & Gardner, L. (2015). Description of stress–strain curves for stainless steel alloys. Materials & Design, 87, 540-552.

[22] Li, D., Paradowska, A., Uy, B., Wang, J., & Khan, M. (2020). Residual stresses of box and I-shaped columns fabricated from S960 ultra-high-strength steel. Journal of Constructional Steel Research, 166, 105904.

[23] Cao, X., Xu, Y., Kong, Z., Shen, H., & Zhong, W. (2017). Residual stress of 800 MPa high strength steel welded T section: Experimental study. Journal of Constructional Steel Research, 131, 30-37.

[24] Sun, Y., Liang, Y., & Zhao, O. (2019). Testing, numerical modelling and design of S690 high strength steel welded I-section stub columns. Journal of Constructional Steel Research, 159, 521-533.

[25] Liu, J. Z., Chen, S., & Chan, T. M. (2023). Hybrid welded T-section stub columns with Q690 flange and Q355 web: Testing, modelling and design. Engineering Structures, 274, 115142.

[26] Yuan, H. X., Wang, Y. Q., Shi, Y. J., & Gardner, L. (2014). Residual stress distributions in welded stainless steel sections. Thin-Walled Structures, 79, 38-51.

[27] Zheng, B., Yang, S., Jin, X., Shu, G., Dong, S., & Jiang, Q. (2020). Test on residual stress distribution of welded S600E high-strength stainless steel sections. Journal of Constructional Steel Research, 168, 105994.

[28] Su, A., Sun, Y., Liang, Y., & Zhao, O. (2021). Membrane residual stresses and local buckling of S960 ultra-high strength steel welded I-section stub columns. Thin-Walled Structures, 161, 107497.

[29] BSK 99 (1999). Swedish regulations for steel structures. Boverkets handbok om stalkonstructioner. Karlskrona, Sweden, 1999.

[30] ECCS. (1976) European convention for constructional steelwork: convention Europeenne de la construction metallique.

[31] Xiong, X., Lu, M., & Lu, Y. (2022). Numerical simulation of longitudinal residual stress distribution in welded T-section of Q690 high strength steel. Journal of Taiyuan University of Technology, 54(1), 107-116. (in Chinese)

[32] Ziemian, R. D. (2010). Guide to stability design criteria for metal structures. John Wiley & Sons.

[33] Schafer, B. W., & Peköz, T. (1998). Computational modeling of cold-formed steel: characterizing geometric imperfections and residual stresses. Journal of Constructional Steel Research, 47(3), 193-210.

[34] Karlsson Hibbitt, Inc Sorensen, ABAQUS/Standard user’s Manual Volumes I-III and ABAQUS CAE Manual. Version 6.14, Pawtucket (USA) 2014.

[35] Schafer, B. W., & Adany, S. (2006). Buckling analysis of cold-formed steel members using CUFSM: conventional and constrained finite strip methods. The 18th International Specialty Conference on Cold-Formed Steel Structures, Orlando, 39-54.

Figures:

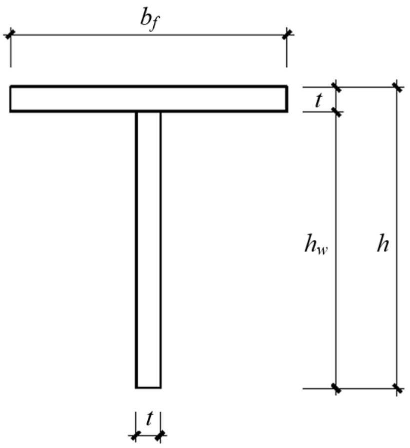

Fig. 1. Notations of LWSS T-section.

Fig. 2. Material test rig.

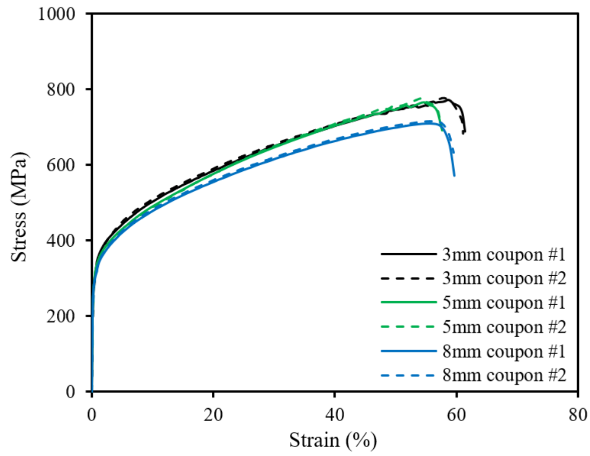

Fig. 3. Measured stress–strain curves.

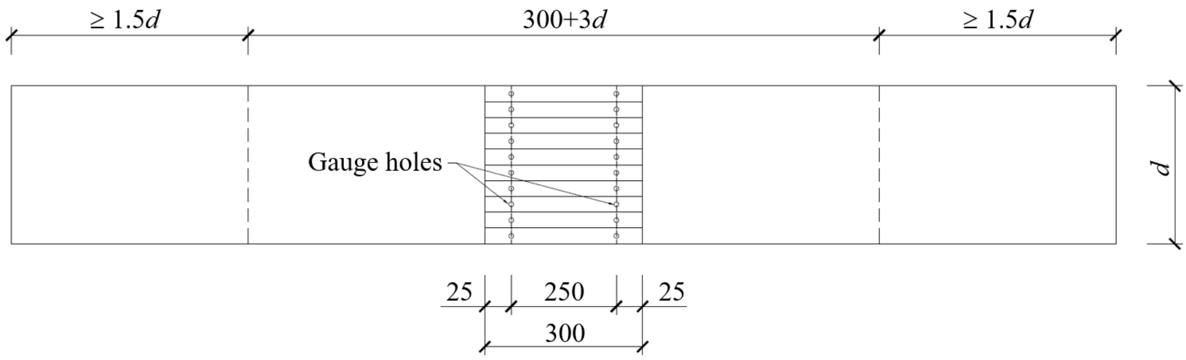

Fig. 4. Illustration of strips cut for residual stress measurements (dimensions in mm).

Fig. 5. Sectioned T-90×90×3 specimen.

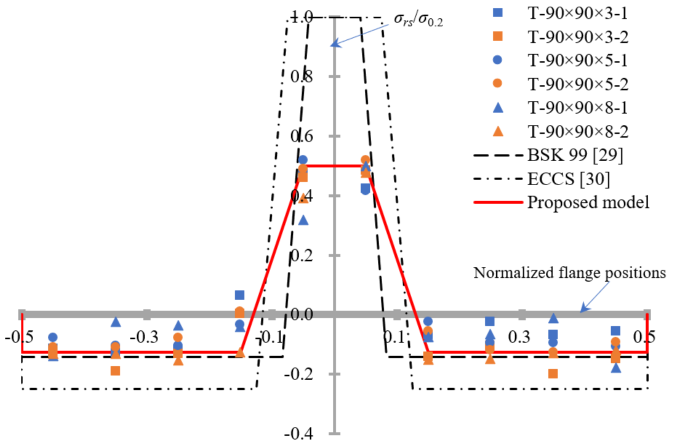

(a) Web.

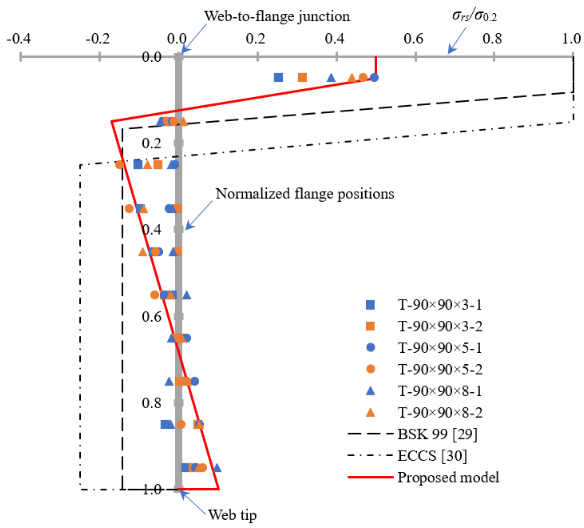

(b) Flange.

Fig. 6. Comparison of measured residual stresses and predictive models. (Note: Positive and negative values represent tensile and compressive residual stresses, respectively.)

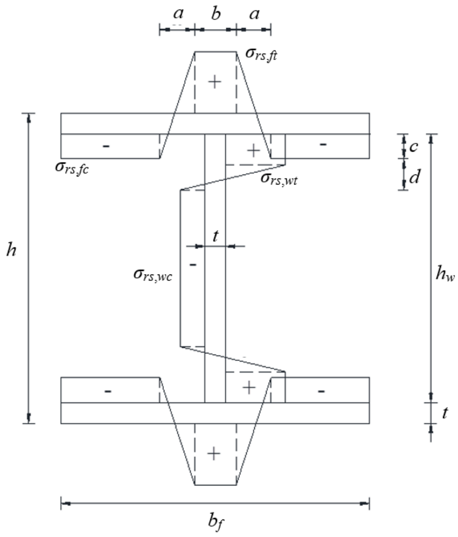

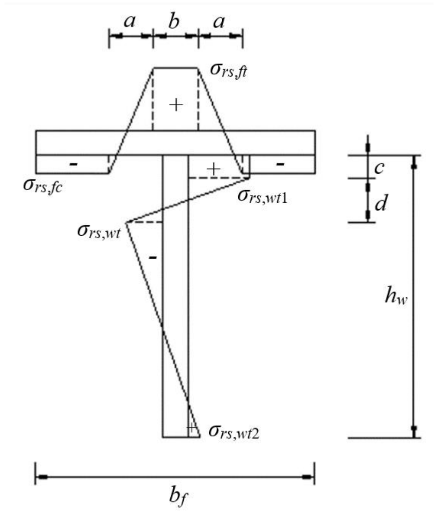

Fig. 7. BSK and ECCS codified residual stress predictive model for I-sections [27,28].

Fig. 8. Proposed predictive model for LWSS T-sections.

Fig. 9. Geometric imperfection measurement rig.

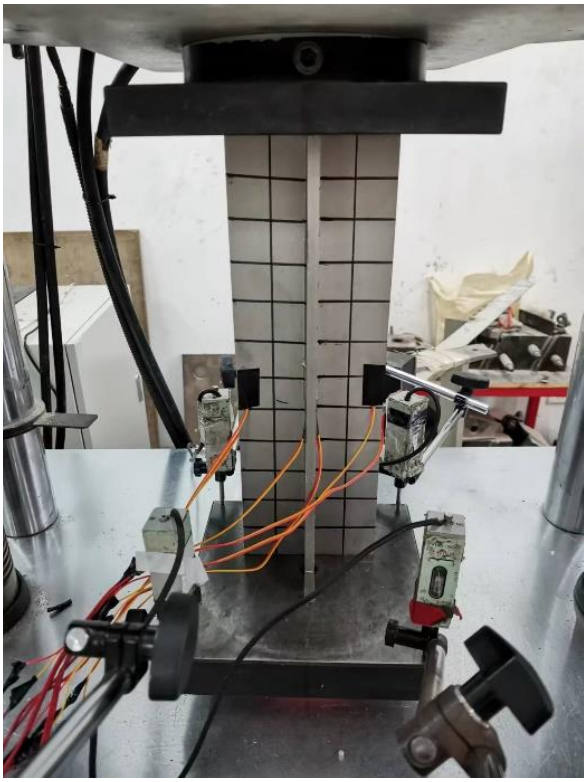

Fig. 10. Stub column test rig.

461

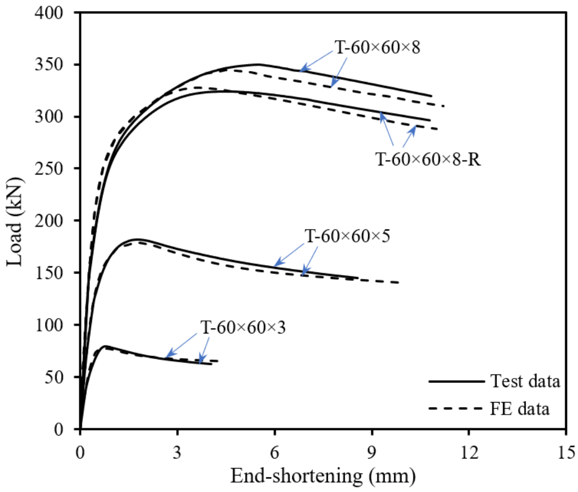

(a) T-60×60 specimens

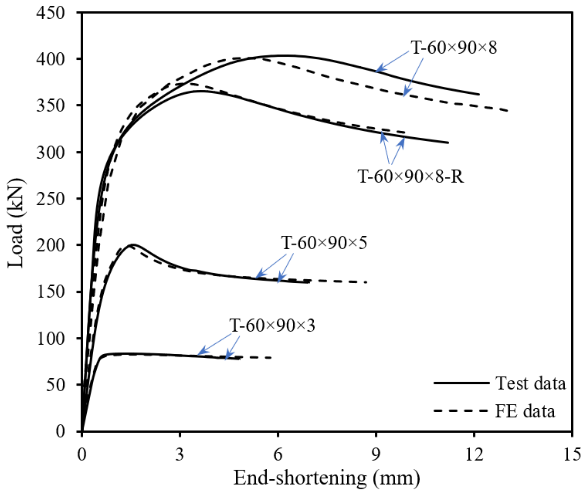

(b) T-60×90 specimens

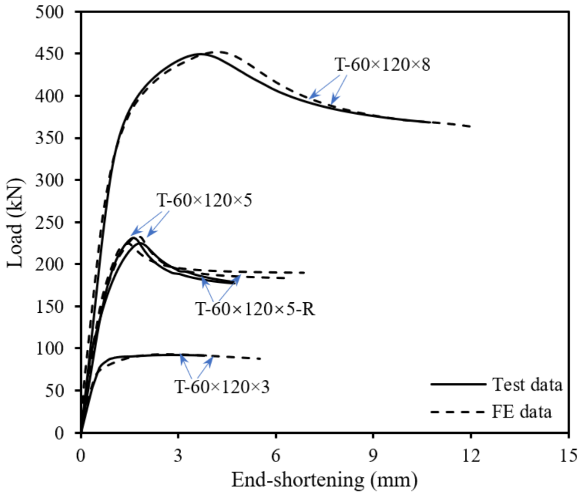

(c) T-60×120 specimens

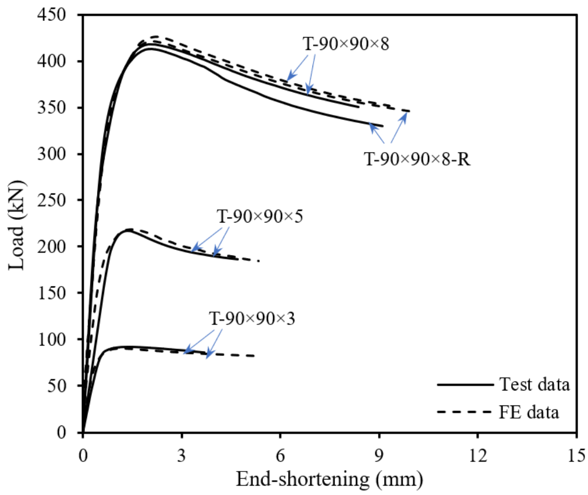

(d) T-90×90 specimens

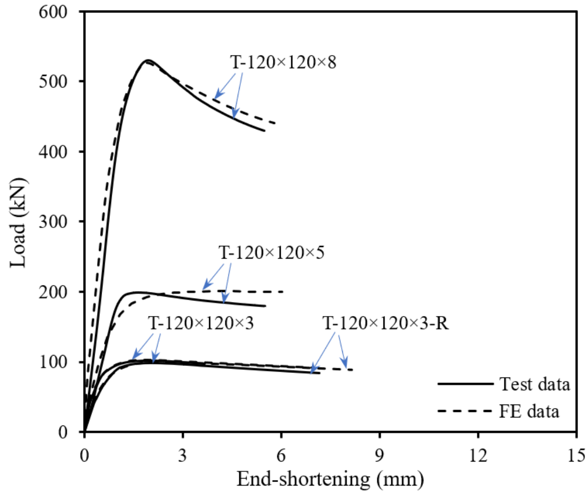

(e) T-120×120 specimens

Fig. 11. Test and FE load–end-shortening curves.

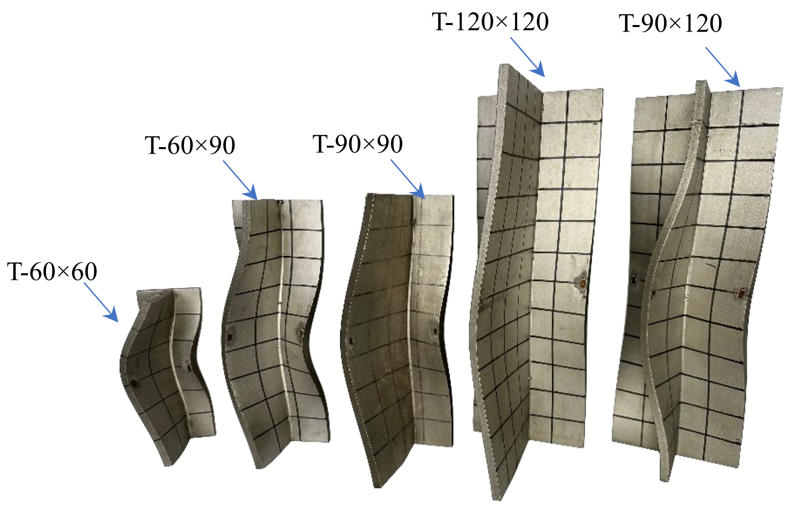

Fig. 12. Failure modes of typical stub column specimens.

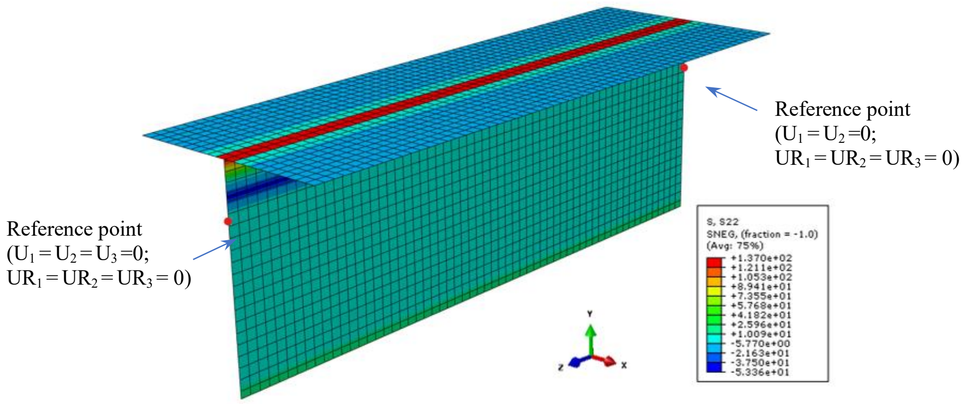

Fig. 13. Residual stresses (in MPa) and boundary conditions for modeled specimen T-60×60×3.

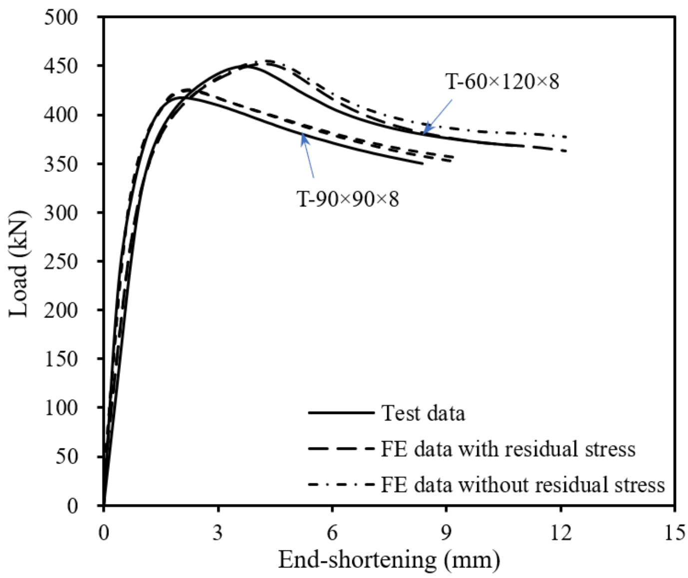

Fig. 14. Evaluation of effect of residual stresses.

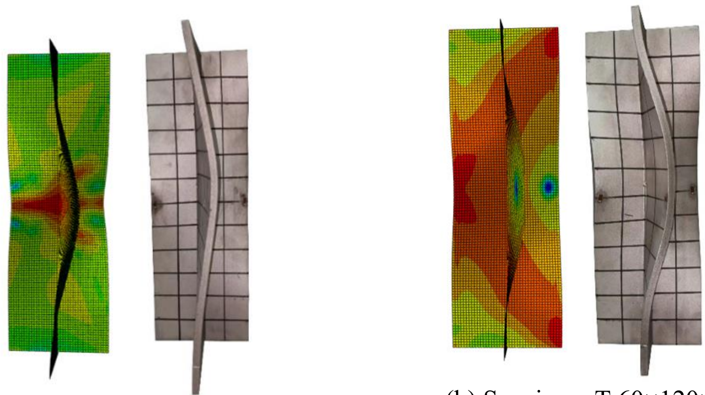

(a) Specimen T-120×120×3 (b) Specimen T-60×120×8

Fig. 15. FE and test failure modes of typical stub column specimens.

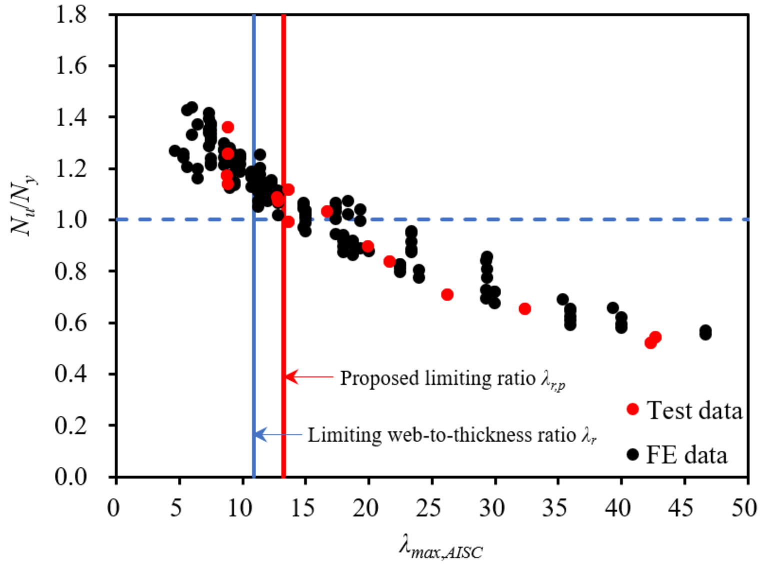

Fig. 16. Assessment of AISC limiting width-to-thickness ratio.

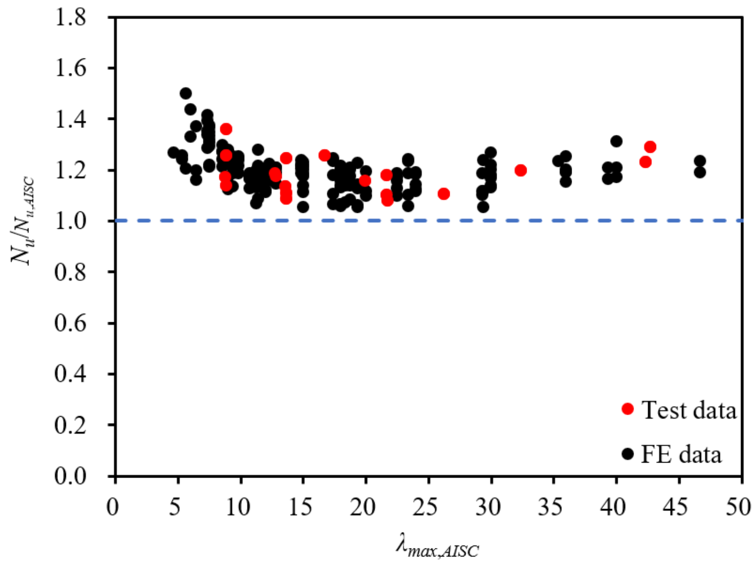

Fig. 17. Comparison of FE/test ultimate loads with AISC predicted ultimate loads.

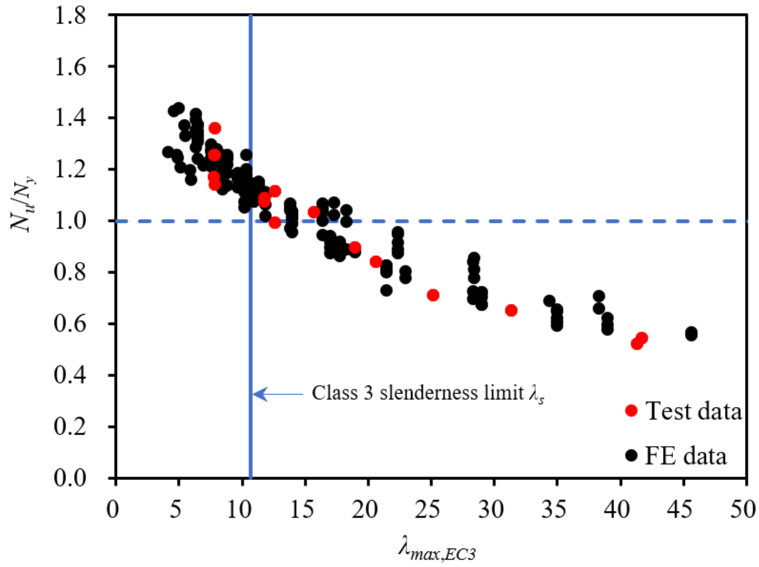

Fig. 18. Assessment of EC3 Class 3 slenderness ratio.

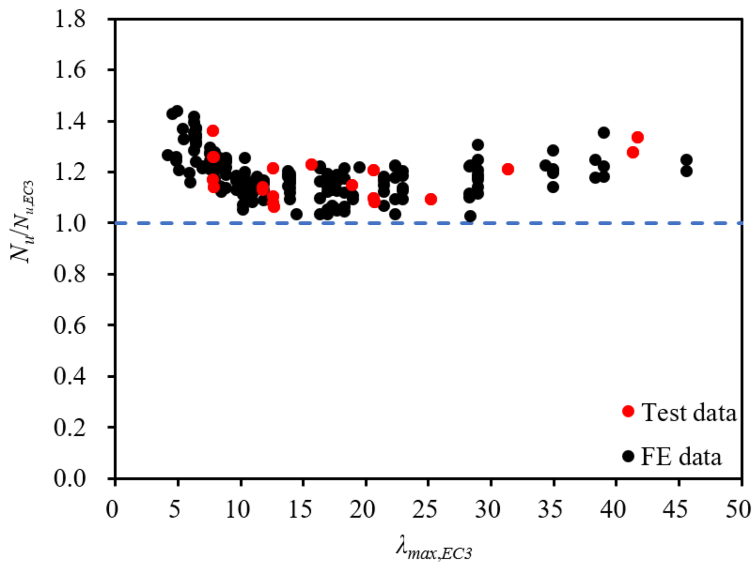

Fig. 19. Comparison of FE/test ultimate loads with EC3 predicted ultimate loads.

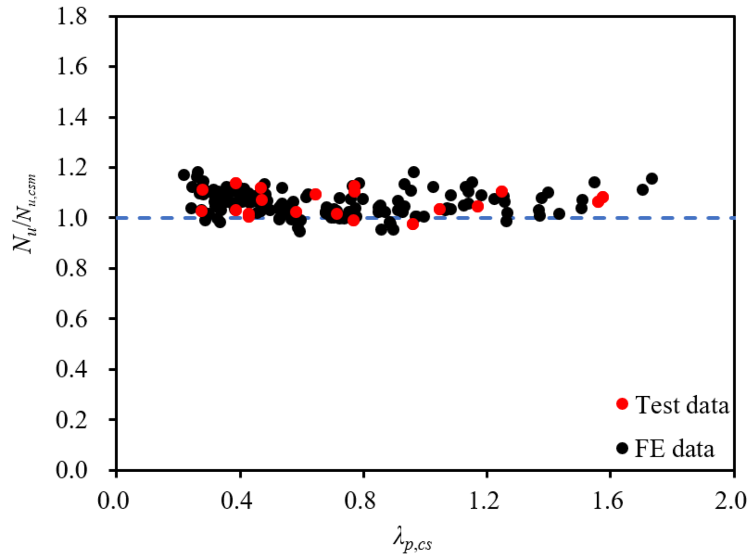

Fig. 20. Comparison of FE/test ultimate loads with CSM predicted ultimate loads.

Tables:

Table 1
Geometric dimensions and test results of stub column specimens.

Specimen	L (mm)	h (mm)	h_w (mm)	b_f (mm)	t (mm)	ω_o (mm)	N_u (kN)	δ_u (mm)
T-60×60×3	179.5	62.4	59.5	59.8	2.89	0.04	79.0	0.76
T-60×60×5	179.4	64.5	59.8	60.9	4.74	0.05	182.1	1.74
T-60×60×8	179.4	67.4	59.8	60.7	7.62	0.09	350.4	5.51
T-60×60×8-R	179.4	67.3	59.7	60.7	7.63	0.05	324.2	4.32
T-60×90×3	269.4	62.5	59.6	89.6	2.89	0.03	83.2	1.35
T-60×90×5	269.5	64.5	59.8	89.6	4.73	0.03	200.5	1.62
T-60×90×8	269.4	67.8	60.2	89.5	7.64	0.10	403.4	5.88
T-60×90×8-R	269.5	67.8	60.2	89.5	7.64	0.04	365.6	3.73
T-60×120×3	359.1	62.7	59.8	119.8	2.89	0.06	92.5	1.01
T-60×120×5	359.5	64.4	59.7	119.9	4.74	0.03	230.9	1.62
T-60×120×5-R	359.5	64.4	59.7	119.8	4.73	0.07	225.5	1.79
T-60×120×8	359.4	67.1	59.5	119.8	7.63	0.11	449.4	3.80
T-90×90×3	269.8	92.7	89.8	89.6	2.87	0.07	91.9	1.02

T-90×90×5	269.9	94.3	89.6	89.6	4.73	0.03	217.2	1.35
T-90×90×8	269.9	97.5	89.9	89.8	7.63	0.06	418.0	1.99
T-90×90×8-R	269.9	97.5	89.9	89.8	7.62	0.03	412.9	2.09
T-120×120×3	359.5	122.7	119.8	119.7	2.88	0.09	102.1	1.25
T-120×120×3-R	359.5	122.7	119.8	119.6	2.90	0.08	98.5	1.38
T-120×120×5	359.9	124.2	119.5	119.5	4.73	0.05	229.1	1.80
T-120×120×8	359.7	127.4	119.8	119.9	7.63	0.06	530.4	2.11

Table 2
Key measured material properties.

Plate thickness (mm)	E (GPa)	$\sigma_{0.2}$ (MPa)	$\sigma_{1.0}$ (MPa)	σ_u (MPa)	ε_u (%)	ε_f (%)	R–O coefficients n	$m_{1.0}$
3	191.8	274	358	754	54	62	6.3	2.0
5	192.3	286	351	774	53	59	6.8	2.0
8	186.8	281	344	715	53	62	7.6	2.1

Table 3
Codified residual stress predictive models for carbon steel welded I-sections.

Predictive model	$\sigma_{rs,ft} = \sigma_{rs,wt}$ (tension)	$\sigma_{rs,fc} = \sigma_{rs,wc}$ (compression)	a	b	c	d
BSK 99 [27]	$\sigma_{0.2}$	From equilibrium	$0.75t$	$1.5t$	$1.5t$	$1.5t$
ECCS [28]	$\sigma_{0.2}$	$0.25\sigma_{0.2}$	$0.05b_f$	$0.15b_f$	$0.075h_w$	$0.05h_w$

Note: (i) The subscripts 'w' and 'f' represent web and flange, respectively.
(ii) The subscripts 't' and 'c' represent tension and compression, respectively.

Table 4
Proposed residual stress predictive model for LWSS T-sections.

$\sigma_{rs,ft} = \sigma_{rs,wt1}$ (tension)	$\sigma_{rs,wt2}$ (tension)	$\sigma_{rs,fc} = \sigma_{rs,wc}$ (compression)	a	b	c	d
$0.5\sigma_{0.2}$	$0.1\sigma_{0.2}$	From equilibrium	$0.1b_f$	$0.1b_f$	$0.05h_w$	$0.1h_w$

Table 5
Comparisons of FE/test ultimate loads with predicted ultimate loads.

(a) AISC 370 [14]				
Cross-section	Test data	FE data	$N_u/N_{u,AISC}$	
			Mean	COV
Non-slender	5	51	1.26	0.067
Slender	15	118	1.17	0.048
Overall	20	169	1.20	0.064
(b) EN 1993-1-4 [15]				
Cross-section	Test data	FE data	$N_u/N_{u,EC3}$	

			Mean	COV
Non-slender	5	64	1.23	0.072
Slender	15	105	1.15	0.054
Overall	20	169	1.18	0.070
(c) CSM [16]				
Cross-section	Test data	FE data	$N_u/N_{u,csm}$	
			Mean	COV
Non-slender	5	64	1.08	0.038
Slender	15	105	1.04	0.043
Overall	20	169	1.06	0.045

Appendix – Worked example

A worked example is presented in this section to demonstrate the calculation procedures of AISC 370, EN 1993-1-4 and the CSM for the design of LWSS T-sections under compression and show the levels of their design accuracy. The calculation is carried out for a typical tested T-section stub column specimen T-120×120×3. The measured cross-section geometric and material properties for this specimen have been reported in Tables 1 and 2 and also presented as follows: h_w = 119.8 mm, b_f = 119.7 mm, t = 2.88 mm, $\sigma_{0.2}$ = 274 MPa, σ_u = 754 MPa and E = 191.8 GPa. The ultimate load is N_u = 102.1 kN; the Poisson's ratio v = 0.3 for stainless steel.

(I) AISC 370 [14]

Step 1: Classification of cross-section

The AISC limiting width-to-thickness ratio $\lambda_r = 0.41\sqrt{\dfrac{E}{\sigma_{0.2}}} = 0.41\times\sqrt{\dfrac{191.8\times10^3}{274}} = 10.9$

The width-to-thickness ratio of web $\lambda_{w,AISC} = \dfrac{h_w + t}{t} = \dfrac{119.8+2.88}{2.88} = 42.7 \geq \lambda_r = 10.9$

The width-to-thickness ratio of flange $\lambda_{f,AISC} = \dfrac{0.5b_f}{t} = \dfrac{0.5\times119.7}{2.88} = 20.8 \geq \lambda_r = 10.9$

Both the web and the flange are slender plate elements; therefore, the examined T-120×120×3 is a slender T-section.

Step 2: Determination of effective widths

The elastic local buckling stress of the slender web

$$f_{el,w} = \frac{0.425\pi^2 E}{12\left(1-\nu^2\right)\lambda_{w,AISC}{}^2} = \frac{0.425\pi^2 \times 191.8\times10^3}{12\times\left(1-0.3^2\right)\times 42.7^2} = 40.4$$

The reduction factor for the slender web

$$\rho_{w,AISC} = 0.772\left(1-0.10\sqrt{\frac{f_{el}}{\sigma_{0.2}}}\right)\sqrt{\frac{f_{el}}{\sigma_{0.2}}} = 0.772\left(1-0.10\sqrt{\frac{40.4}{274}}\right)\sqrt{\frac{40.4}{274}} = 0.28$$

The effective width of the web $h_{w,eff} = \rho_{w,AISC} h_w = 0.28\times119.8 = 33.5$ mm

The elastic local buckling stress of the slender flange

$$f_{el,f} = \frac{0.425\pi^2 E}{12\left(1-\nu^2\right)\lambda_{f,AISC}{}^2} = \frac{0.425\pi^2 \times 191.8\times10^3}{12\times\left(1-0.3^2\right)\times 20.8^2} = 170.6$$

The reduction factor for the slender flange

$$\rho_{f,AISC} = 0.772\left(1-0.10\sqrt{\frac{f_{el}}{\sigma_{0.2}}}\right)\sqrt{\frac{f_{el}}{\sigma_{0.2}}} = 0.772\left(1-0.10\sqrt{\frac{170.6}{274}}\right)\sqrt{\frac{170.6}{274}} = 0.56$$

The effective width of the flange $b_{f,eff} = \rho_{f,AISC} b_f = 0.56\times119.7 = 67.0$ mm

Step 3: Calculation of AISC design compression resistance

The AISC effective area of the slender T-section

$$A_{eff,AISC} = h_{w,eff}t + b_{f,eff}t = 33.5\times2.88 + 67.0\times2.88 = 288.6 \text{ mm}^2$$

The AISC design compression resistance of the slender T-section

$$N_{u,AISC} = A_{eff,AISC}\sigma_{0.2} = 288.6\times274/1000 = 79.1 \text{ kN}$$

$$\frac{N_u}{N_{u,AISC}} = \frac{102.1}{79.1} = 1.30$$

(II) EN 1993-1-4 [15]

Step 1: Classification of cross-section

The EC3 Class 3 slenderness limit $\lambda_s = 1.15\sqrt{\frac{235}{\sigma_{0.2}}} = 11.5\times\sqrt{\frac{235}{274}} = 10.7$

The slenderness of web $\lambda_{w,EC3} = \frac{h_w}{t} = \frac{119.8}{2.88} = 41.7 \geq \lambda_s = 10.7$

The slenderness of flange $\lambda_{f,EC3} = \frac{0.5\left(b_f - t\right)}{t} = \frac{0.5\times\left(119.7-2.88\right)}{2.88} = 20.3 \geq \lambda_s = 10.7$

Both the web and the flange are slender plate elements; therefore, the examined T-120×120×3 is a Class 4 slender T-section.

<u>Step 2: Determination of effective widths</u>

The element slenderness of the slender web

$$\lambda_{p,w} = \frac{\lambda_{w,EC3}}{18.2\sqrt{235/\sigma_{0.2}}} = \frac{41.7}{18.2\times\sqrt{235/274}} = 2.48$$

The reduction factor for the slender web

$$\rho_{w,EC3} = \frac{0.655\lambda_{p,w} - 0.013}{\lambda_{p,w}{}^2} = \frac{0.655\times 2.48 - 0.013}{2.48^2} = 0.26$$

The effective width of the web $h_{w,eff} = \rho_{w,EC3} h_w = 0.26\times 119.8 = 31.1$ mm

The element slenderness of the slender flange

$$\lambda_{p,f} = \frac{\lambda_{f,EC3}}{18.2\sqrt{235/\sigma_{0.2}}} = \frac{20.3}{18.2\times\sqrt{235/274}} = 1.21$$

The reduction factor for the slender flange

$$\rho_{f,EC3} = \frac{0.655\lambda_{p,f} - 0.013}{\lambda_{p,f}{}^2} = \frac{0.655\times 1.21 - 0.013}{1.21^2} = 0.54$$

The effective width of the flange

$$b_{f,eff} = \rho_{f,EC3}\left(b_f - t\right) + t = 0.54\times\left(119.7 - 2.88\right) + 2.88 = 66.0 \text{ mm}$$

<u>Step 3: Calculation of EC3 design compression resistance</u>

The EC3 effective area of the slender T-section

$$A_{eff,EC3} = h_{w,eff}t + b_{f,eff}t = 31.1 \times 2.88 + 66.0 \times 2.88 = 279.7 \text{ mm}^2$$

The AISC design compression resistance of the slender T-section

$$N_{u,EC3} = A_{eff,EC3}\sigma_{0.2} = 279.7 \times 274/1000 = 76.6 \text{ kN}$$

$$\frac{N_u}{N_{u,EC3}} = \frac{102.1}{76.6} = 1.33$$

(III) CSM [16]

Step 1: Determination of CSM strain limit

The elastic local buckling stress of the T-section is derived using the finite-strip package CUFSM [35] $\sigma_{cr,cs} = 110.2$ MPa

The cross-section slenderness $\lambda_{p,cs} = \sqrt{\dfrac{\sigma_{0.2}}{\sigma_{cr,cs}}} = \sqrt{\dfrac{274}{110.2}} = 1.58$

For $\lambda_{p,cs} = 1.58 > 0.68$, $\dfrac{\varepsilon_{csm}}{\varepsilon_y} = \left(1 - \dfrac{0.222}{\lambda_{p,cs}^{1.05}}\right)\dfrac{1}{\lambda_{p,cs}^{1.05}} = \left(1 - \dfrac{0.222}{1.58^{1.05}}\right)\dfrac{1}{1.58^{1.05}} = 0.53$

Step 2: Calculation of CSM design compression resistance

For $\dfrac{\varepsilon_{csm}}{\varepsilon_y} = 0.53 < 1.0$,

the CSM design compression resistance of the slender T-section

$$N_{u,csm} = A\sigma_{0.2}\frac{\varepsilon_{csm}}{\varepsilon_y} = 688.4 \times 274 \times 0.53/1000 = 100.0 \text{ kN}$$

$$\frac{N_u}{N_{u,csm}} = \frac{102.1}{100} = 1.02$$